Dynamics Inherent in Helix 27 from *Escherichia coli* 16S Ribosomal RNA†

John A. H. Hoerter, Meredith Newby Lambert, Miguel J. B. Pereira, and Nils G. Walter*

Department of Chemistry, University of Michigan, 930 North University Avenue, Ann Arbor, Michigan 48109-1055

Received July 11, 2004; Revised Manuscript Received September 9, 2004

ABSTRACT: The original interpretation of a series of genetic studies suggested that the highly conserved *Escherichia coli* 16S ribosomal RNA helix 27 (H27) adopts two alternative secondary structure motifs, the 885 and 888 conformations, during each cycle of amino acid incorporation. Recent crystallographic and genetic evidence has called this hypothesis into question. To ask whether a slippery sequence such as that of H27 may harbor inherent conformational dynamics, we have designed a series of model RNAs based on *E. coli* H27 for *in vitro* physicochemical studies. One-dimensional ^{1}H NMR spectroscopy demonstrates that both the 885 and 888 conformations are occupied to approximately the same extent ($f_{888} = 0.427 \pm 0.04$) in the native H27 sequence at low pH (6.4) and low ionic strength (50 mM NaCl). UV irradiation assays conducted under conditions analogous to those used for assays of ribosomal function (pH 7.5 and 20 mM $MgCl_2$) suggest that nucleotides 892 and 905, which are too far apart in the known 885 crystal structures, can approach each other closely enough to form an efficient cross-link. The use of a fluorescence resonance energy transfer (FRET)-labeled RNA together with a partially complementary DNA oligonucleotide that induces a shift to the 888 conformation shows that H27 interchanges between the 885 and 888 conformations on the millisecond time scale, with an equilibrium constant of 0.33 ± 0.12. FRET assays also show that tetracycline interferes with the induced shift to the 888 conformation, a finding that is consistent with crystallographic localization of tetracycline bound to the 885 conformation of H27 in the 30S ribosomal subunit. Taken together, our data demonstrate the innate tendency of an isolated H27 to exist in a dynamic equilibrium between the 885 and 888 conformations. This begs the question of how these inherent structural dynamics are suppressed within the context of the ribosome.

The ribosome is the universal protein biosynthesis machine. As such, it exhibits a high degree of structural organization which gives rise to orchestrated dynamic motions involved in the process of translation. Numerous large-scale structural rearrangements have been visualized by trapping and subsequent cryoelectron microscopy of intermediate functional states (*1*, *2*). For example, upon binding of elongation factor G (EF-G),[1] a large conformational reorganization is observed in which the small and large ribosomal subunits undergo a relative ratchet-like motion in conjunction with many local conformational changes, facilitating the translocation of the messenger RNA (mRNA) and A- and P-site transfer RNAs (tRNAs) (*3*−*7*). The limited resolution of the cryo-EM maps (up to ∼10 Å), however, prevents elucidation of the link between the observed global movement of the subunits and their local molecular reorganization. By contrast, recent advances in X-ray crystallographic analysis of ribosomal subunits have provided a wealth of atomic-resolution, yet largely static, structural information (*8*−*10*). Clearly, 16S ribosomal RNA (rRNA) is a central player in these structural rearrangements. It is the primary interaction partner for messenger RNA; it is responsible for message decoding and proofreading which enable subsequent peptidyl transfer; and it appears to undergo substantial shape changes, including an opening and closing motion upon cognate tRNA selection (*11*, *12*). While recent normal-mode analyses on simplified models suggest that shape-dependent dynamic properties of the global architecture may provide the framework for large-scale conformational changes in the ribosome (*6*), details of the temporal and spatial coordination between local and global rearrangements are not well understood.

Helix 27 (H27) of 16S rRNA (comprising nucleotides 885−912 in *Escherichia coli* 16S rRNA) is a highly conserved RNA motif in the central domain of small subunit RNA. It lies on the axis of the intersubunit ratchet motion in a location of potentially large conformational dynamics (*6*) (Figure 1); it is packed against the decoding center in helix 44 that senses and reports on correct tRNA selection; and its tetraloop acts as an intersubunit bridge (*4*−*6*, *8*, *9*, *13*). All of these observations are suggestive of a potential key role of H27 in ribosome dynamics and function, and more specifically in the linkage between correct codon recognition and the resulting cascade of steps that ultimately

† This work was supported by NIH Grant GM62357, American Chemical Society Petroleum Research Fund Grant 37728-G7, and Dow Corning Assistant Professorship and Camille Dreyfus Teacher-Scholar Awards to N.G.W., by NIH Molecular Biophysics Training Grant predoctoral fellowships to J.A.H.H. and M.J.B.P., and by an NIH Ruth L. Kirschstein NRSA postdoctoral fellowship to M.N.L.

* To whom correspondence should be addressed. Phone: (734) 615-2060. Fax: (734) 647-4865. E-mail: nwalter@umich.edu.

[1] Abbreviations: FRET, fluorescence resonance energy transfer; NMR, nuclear magnetic resonance; rRNA, ribosomal RNA; H27, helix 27; EF-G, elongation factor G; tRNA, transfer RNA; mRNA, messenger RNA; EDTA, ethylenediaminetetraacetic acid; cryo-EM, cryoelectron microscopy; SDS, sodium dodecyl sulfate; DTT, dithiothreitol; NOE, nuclear Overhauser effect; HSQC, heteronuclear single-quantum correlation.

10.1021/bi048533y CCC: $27.50
Published on Web 10/28/2004

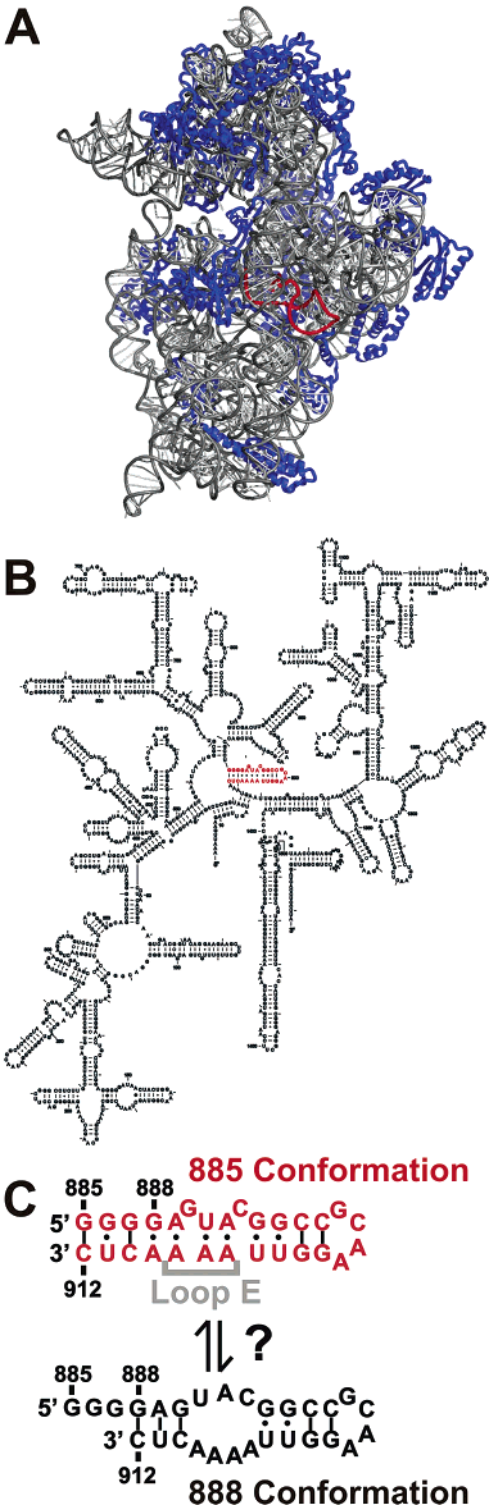

FIGURE 1: Helix 27 (H27, nucleotides 885−912) in the central domain of *E. coli* 16S rRNA. (A) Location of H27 in the crystal structure of the 30S ribosomal subunit (PDB entry 1FJF) (*8*), as viewed from the interface with the 50S subunit. H27 is colored red and the remainder of the 16S rRNA gray, and the small subunit proteins are colored blue. This representation of the 30S subunit was created with Nuccyl version 1.4 (http://www.mssm.edu/students/jovinl02/research/nuccyl.html) and rendered with MacPyMOL (DeLano Scientific, San Carlos, CA). (B) Secondary structure of the 16SrRNA, with H27 highlighted in red (*77*). (C) The 885 conformation, observed in all crystal structures of the 30S ribosomal subunit, is characterized by an 885·912 base pair and the seven-nucleotide loop E motif, whereas a proposed alternative base pairing scheme, the 888 conformation, manifests in an 888·912 base pair.

result in translocation. Evolutionary conservation was originally used to predict a base pair between G888 and C912 (*14*), but is also consistent with base pairing between G885 and C912 given the fact that the 3′-most CUC triplet can pair with either the 5′-most GGG or the subsequent GAG triplet by a simple three-nucleotide slippage (Figure 1) (*15*). Dahlberg and co-workers, inspired by the finding from Stutz and co-workers that a C912U mutation conferred streptomycin resistance, isolated mutants that suppress the effects of a deleterious C912G mutant in *E. coli* (*16*, *17*). They demonstrated that a compensatory mutation, G885C, restored growth rates to levels near those of the wild type, experimentally supporting the 912-885 base pairing scheme (*18*). Subsequently, the same group introduced mutations into 16S rRNA to selectively stabilize either the 912-885 or the 912-888 base pairing scheme (henceforth termed the 885 or 888 conformation, respectively) and tested for a resulting phenotype in *E. coli* (*19*). In conjunction with cryoelectron microscopy studies of the mutated ribosomes, this work supported the notion that H27 cycles between the 885 and 888 conformations during translation and that this local conformational switch impacts the accuracy of A site tRNA decoding by triggering numerous changes in global ribosome architecture (*20*). However, only the 885 conformation has been observed in all functional ribosome states investigated by X-ray crystallography to date (*9*, *11*, *12*, *21*−*23*), where it appears to be stabilized by the common loop E motif (*24*).

This discrepancy prompted Dahlberg and co-workers to reexamine their genetic approach. They found that two secondary mutations, C1192U in 16S RNA and A2058G in 23S RNA, introduced as genetic markers and initially thought to be silent, had "synergistic effects" with mutations in H27. In the absence of these secondary mutations, an *E. coli* strain that produces mutant ribosomes incapable of adopting the 888 conformation exhibits essentially the same growth rate as the wild type, calling into question the original switch helix hypothesis (*23*).

With this recent change in the interpretation of the existing genetic, biochemical, and structural data, a number of questions arise. Is a slippery sequence such as that of H27 indeed trapped in only one conformational state, the 885 conformation? Or is conformational exchange still occurring, and at what rate? Given that base pairs in RNA can be as short-lived as sub-milliseconds (*25*, *26*), it is possible that conformational exchange of a slippery sequence may actually be quite rapid. Insight into the kinetics and thermodynamics of such conformational exchange will not only help elucidate local structural dynamics in the ribosome but also shed light on conformational changes in slippery sequences involved in biological processes such as ribosomal frameshifting (*27*) or substrate recognition in the *Neurospora* VS ribozyme (*28*).

Here, we have used the isolated H27 sequence to define a kinetic and thermodynamic framework of conformational exchange between the 885 and 888 conformations. Similar studies of isolated structural motifs from the ribosome have previously led to fundamental insights into the hierarchical assembly of the central domain of the 30S subunit (*29*), the mechanism of decoding and its modulation by antibiotics (*30*), and the thermodynamic stability of novel RNA motifs discovered in the ribosomal crystal structures (*31*). Utilizing a complementary set of techniques, including ^{1}H NMR spectroscopy, UV-induced photo-cross-linking, and steady-

state fluorescence resonance energy transfer (FRET) spectroscopy, we find that the isolated H27, under a variety of ionic conditions, exists in a dynamic equilibrium between the 885 and 888 conformers with millisecond exchange times and an equilibrium constant close to 1. FRET assays also show that the antibiotic tetracycline appears to specifically interfere with an induced shift toward the 888 conformation, a finding that is consistent with crystallographic localization of tetracycline bound to the 885 conformation of H27 in the 30S ribosomal subunit and that may pertain to tetracycline's mode of action. Taken together, our results invoke the notion of a structurally very dynamic helix 27 and beg the question of how these inherent structural dynamics are suppressed within the ribosome.

MATERIALS AND METHODS

RNA and DNA Preparation. Three different RNA constructs derived from H27 of *E. coli* 16S rRNA were generated for our NMR studies. The *Native* construct (5′-GGG GAG UAC GGC CGC AAG GUU AAA ACU C-3′) represents the unmodified *E. coli* H27 sequence, comprising nucleotides 885−912. RNA constructs *885* (5′-GGG GAG UAC GGC CGC AAG GUU AAA ACC C-3′) and *888* (5′-GGG GAG UAC GGC CGC AAG GUU AAA ACU CCC C-3′) were designed to specifically represent the H27 912-885 and 912-888 base pairing schemes, respectively (Figure 1). These constructs suppress slippage of the base pairs at the helix terminus through a U911C mutation in the *885* construct, thus affording three stable G·C pairs in the 885 conformation versus a destabilizing A·C mismatch in the 888 conformation, and through extending the terminal helix of the *888* construct by three G·C base pairs that only can form in the 888 conformation. The constructs were runoff transcribed from double-stranded DNA templates containing an upstream T7 RNA polymerase promoter. Transcription reaction mixtures contained 40 mM Tris-HCl (pH 7.5), 15 mM $MgCl_2$, 5 mM dithiothreitol (DTT), 2 mM spermidine, rNTPs (4 mM each), 5 units/mL inorganic pyrophosphatase, and 0.1 mg/mL T7 RNA polymerase [purified in the His-tagged form from an overexpressing strain as described previously (*32*)] and were incubated at 37 °C overnight (∼16 h). The full-length transcript was isolated after denaturing, 8 M urea, 20% (w/v) polyacrylamide gel electrophoresis by UV shadowing, diffusion elution of small gel slices into 5 mM EDTA, and ethanol precipitation. For NMR, the RNA was further purified by anion exchange chromatography on Sephadex A-25 (Sigma), and dialysis into NMR buffer [10 mM Na_iPO_4 (pH 6.4), 0.1 mM EDTA, and 50 mM NaCl] by ultrafiltration using Centricon-3 concentrators (Amicon). Samples were concentrated to approximately 200 μL, and NMR buffer was added to a final volume of 225−250 μL, including the addition of a 5% final volume of 99.9% D_2O (Aldrich or Cambridge Isotope Labs) for lock. Final RNA concentrations ranged from 0.5 to 1.2 mM as measured by UV absorption, where 1 A_{260} unit equals 37 μg of RNA/mL. Microvolume NMR tubes (Shigemi) were used for NMR data collection.

RNA construct *EH27* (5′-CCG CCU GGG GAG UAC GGC CGC AAG GUU AAA ACU C-3′) for UV cross-linking experiments contains an extended H27 sequence (nucleotides 879−912) in which a 5′-overhang facilitates the binding of DNA oligonucleotides. It was synthesized by Dharmacon, Inc. (Lafayette, CO), deprotected as recommended by the manufacturer, purified on a denaturing 8 M urea, 20% (w/v) polyacrylamide gel, eluted into crush and soak buffer [500 mM NH_4OAc, 0.1% sodium dodecyl sulfate (SDS), and 0.1 mM EDTA], chloroform extracted, precipitated as described above, and further purified by C_8 reverse-phase HPLC with a linear acetonitrile gradient in triethylammonium acetate as described previously (*33*, *34*). For determining the binding rate of *9mer* DNA to *EH27*, this construct was 5′-fluorescein labeled to generate construct *5′FEH27*. To this end, *EH27* RNA (final concentration of 0.9−1 μM) was mixed with 5 mM [γ-S]ATP (Sigma) and 1 unit/μL T4 polynucleotide kinase (Takara) in 50 mM Tris-HCl (pH 8.0), 10 mM $MgCl_2$, and 5 mM DTT and incubated at 37 °C for 3 h (*35*). The phosphorothioated RNA was extracted with phenol and chloroform, ethanol precipitated, and desalted using a Centrispin Column (Princeton Separations). It was then diluted to 0.3 μM and mixed with 5 mM fluorescein-5-maleimide (Molecular Probes) in 35 mM Tris-HCl (pH 7.7) and 14% DMSO, incubated at 70 °C for 30 min, ethanol precipitated, and purified by C_8 reverse-phase HPLC (*33*, *34*). Appropriate fractions were pooled and passed over a NAP-5 gel filtration column (Amersham Phamacia Biotech) to yield the final stock solution of *5′FEH27*.

RNA construct *FEH27T* for FRET experiments was synthesized in a singly labeled form by Howard Hughes Medical Institute Biopolymer/Keck Foundation Biotechnology Resource Laboratory at the Yale University School of Medicine (New Haven, CT) with the same sequence as construct *EH27* (5′-CCG CCU GGG GAG UAC GGC CGX AAG GUU AAA ACY C-3′), except the cytidine in the variable position in the GNRA tetraloop and uracil 911, X and Y respectively, were replaced with the uracil analogues Fluorescein dT and Amino-Modifier C6 dT (Glen Research), respectively. This synthetic RNA was deprotected by treatment with triethylammonium trihydrofluoride and purified by denaturing gel electrophoresis and C_8 reverse-phase HPLC as described above (*33*, *34*). It was chloroform extracted and then reacted with tetramethylrhodamine succinimidyl ester (Molecular Probes) in 7.5 mM $Na_2B_4O_7$ and 14% DMSO, incubated at room temperature overnight (∼16 h), repurified by C_8 reverse-phase HPLC, and passed over a NAP-5 column, thus yielding the doubly labeled FRET construct *FEH27T* (*33*, *34*).

The DNA sequences used in this study were as follows: *9mer* (5′-CCC AGG CGG-3′), *F2* (5′-CCC AGG CGG TCG ACT TA-3′), *cF2* (5′-TAA GTC GAC CGC CTG GG-3′), and *Disrupter* (5′-TAC TCC-3′). Oligodeoxynucleotides were synthesized and desalted by Invitrogen (Carlsbad, CA). Synthetic DNA was used as supplied provided that it gave a clear solution upon addition of water and appeared to be homogeneous as judged by denaturing polyacrylamide gel electrophoresis. Otherwise, the material was gel purified as described above. Stock concentrations were determined by UV absorbance as described above for RNA.

NMR Spectroscopy. All NMR spectra were acquired in NMR buffer [10 mM Na_iPO_4 (pH 6.4), 0.1 mM EDTA, and 50 mM NaCl] at 8 °C, unless otherwise noted, on a Varian Inova 800 MHz spectrometer equipped with a triple-resonance ^1H, ^{13}C, ^{15}N probe with *Z*-gradients. Each spectrum was collected using a water flip-back solvent suppression scheme followed by a WATERGATE pulse scheme (*36*, *37*).

Quadrature detection was achieved by implementation of the States−TPPI method in all spectra (*38*). Data for the *888* construct were collected over 54 scans; 2816 complex points were acquired for a sweep width of 20 000 Hz, and a recycle delay of 1.3 s was used. Data for constructs *885* and *Native* were collected in 512 scans with 8000 complex points and a spectral width of 20 000 Hz. A 1.5 s recycle delay was used. Spectra were processed with nmrPipe and visualized with Igor Pro (WaveMetrics) (*39*). Spectra were referenced to the solvent resonance position, 4.97 ppm, at 8 °C. All spectra were processed using a solvent filter and a cosine-bell apodization function. Each FID was zero-filled once before Fourier transformation.

Spectra of the *885*, *888*, and *Native* constructs were baseline corrected and normalized to the Lorentzian fit area of the imino proton resonance arising from U904 (∼11.8 ppm). A calculated spectrum was constructed as a linear combination of the *885* and *888* spectra and minimized against the *Native* spectrum using Levenberg−Marquart least-squares regression as implemented in Igor Pro, using only the relative contribution of the 888 conformation, f_{888} (where $f_{885} = 1 - f_{888}$), as a fitting parameter. The spectral region containing the exchange-broadened hump centered at approximately 11 ppm in the *Native* spectrum was omitted for the fit.

Thermal Denaturation. Melting temperatures (T_m) for the *885*, *888*, and *Native* NMR constructs were determined from thermal denaturation profiles recorded on a Beckman DU640B spectrophotometer equipped with a high-performance temperature controller and a Micro Auto 6 T_m cell holder. RNA samples (1 μM, 300 μL) were prepared in 10 mM sodium phosphate (pH 6.4), 0.1 mM EDTA, and 1.0 M sodium chloride and degassed for 5 min prior to obtaining UV melting curves. The temperature was increased from 15 to 85 °C at a rate of 1 °C/min, and the absorbance at 260 nm was recorded every 0.5 °C. The first derivatives of the resulting melting profiles were fit to Gaussian distributions using the spectrophotometer as well as MicroCal Origin 7.0 software, yielding T_m values as the maxima of the Gaussians. Three independent melting profiles were recorded for each construct to estimate the experimental error in T_m to approximately ±2 °C.

UV-Induced Photo-Cross-Linking. EH27 RNA was 5′-end labeled with [γ-^{32}P]ATP and T4 polynucleotide kinase. In the case of in vitro-transcribed constructs *885* and *888*, a 5-fold excess of *Disrupter* DNA was added to interfere with RNA secondary structure, the mixture heated to 70 °C and cooled to room temperature, the RNA dephosphorylated with calf intestine alkaline phosphatase, extracted with phenol and chloroform, and ethanol precipitated prior to 5′-^{32}P labeling. The radiolabeled *885* and *888* constructs were further purified by denaturing, 8 M urea, 20% (w/v) polyacrylamide gel electrophoresis, elution into 10 mM Tris-HCl (pH 7.6) and 1 mM EDTA overnight, and ethanol precipitation.

5′-^{32}P-labeled *EH27*, *885*, and *888* constructs (<2.5 nM) were annealed in standard buffer as described above. The solutions were incubated in wells of a microplate floating in a circulating water bath at 25 °C. A hand-held UV lamp (λ = 254 nm, Spectroline EF-180C) was positioned ∼1.5 cm above the microplate. Samples were taken at appropriate points over a 120 min time interval, mixed with 10 μL of 80% formamide, 0.025% xylene cyanole, 0.025% bromophenol blue, and 50 mM EDTA, separated from un-cross-linked RNA by denaturing, 8 M urea, 20% (w/v) polyacrylamide gel electrophoresis, and quantified using a Molecular Dynamics Storm 840 phosphorimager. The intensity of the upper of the two UV-induced cross-links was calculated as the fraction of all three bands in the lane, plotted as a function of time, and fit to the single-exponential increase function $y = y_o + A_1(1 - e^{-t/\tau_1})$ to extract a cross-linking rate constant k_{obs} ($=\tau_1^{-1}$). For assignment of the location of the cross-link in *EH27*, unlabeled *EH27* was exposed to UV light, and the upper cross-linked RNA band (*cEH27*) was gel purified, stained with ethidium bromide, and eluted as described above for radiolabeled RNA. It was then 5′-end radiolabeled as described above, or 3′-end labeled using [^{32}P]-pCp and T4 RNA ligase. The RNA was analyzed on an 8 M urea, 15% wedged polyacrylamide sequencing gel, alongside ladders from partial digestion with G-specific RNase T_1 and alkaline hydrolysis of both cross-linked and un-cross-linked *EH27* (*40*).

Steady-State Fluorescence Spectroscopy. Doubly labeled FRET construct *FEH27T* was prepared at 20 nM in standard buffer [50 mM Tris-HCl (pH 7.5), 50 mM NH_4Cl, and 20 mM $MgCl_2$] annealed by heating to 70 °C for 2 min and cooling to room temperature over 10 min. Steady-state fluorescence measurements were performed at 25 °C on an Aminco-Bowman Series 2 (AB2) spectrofluorometer (Thermo Electron Corp.) as described previously (*34*, *41*). The sample (156 μL) was placed in the fluorometer cuvette; fluorescein was excited at 490 nm (4 nm bandwidth), and fluorescence emission was recorded simultaneously at the fluorescein (520 nm, 8 nm bandwidth) and tetramethylrhodamine (585 nm, 8 nm bandwidth) wavelengths via an oscillating monochromator. For the fuel strand experiment, DNA *F2* (1 μL) was manually added to a final concentration of 100 nM. After the signals reached a new equilibrium position, DNA *cF2* (1 μL) was added to a final concentration of 140 nM. The FRET ratio Q ($=F_{585}/F_{520}$) was calculated and its time trace recorded along with the single-fluorophore data. To test the impact of antibiotics on the DNA-induced shift from the 885 conformation to the 888 conformation, tetracycline hydrochloride, streptomycin sulfate (both from ICN Biomedical Inc.), and kanamycin sulfate (Fisher Scientific) were prepared at a stock concentration of 10 mM (used within 24 h; the tetracycline was protected from light). *FEH27T* (40 nM) was annealed as described above in buffer consisting of 600 mM Tris-HCl (pH 7.5), 100 mM NH_4Cl, and 40 mM $MgCl_2$. After being cooled to room temperature, water and an antibiotic stock solution were added to produce a final *FEH27T* concentration of 20 nM in a buffer similar to standard buffer, except that it contained a variable concentration of antibiotic and 300 mM Tris-HCl instead of 50 mM Tris-HCl to stabilize the pH at 7.5. This solution was preincubated at 25 °C for 1−2 min, fluorescence data acquisition initiated as described above, and *9mer* DNA manually added to a final concentration of 400 nM. (Addition and mixing of the DNA took ∼10 s in all cases.) The FRET ratio, Q, of time traces upon *9mer* addition was normalized to its average value before *9mer* addition, Q_0, by calculating $(Q - Q_0)/Q_0$, to yield a relative FRET efficiency, which was fit to the single-exponential increase function as described above to extract the amplitude (A_1) and the rate constant

k_{obs} ($=\tau_1^{-1}$) (*33*, *34*). None of the antibiotics absorb at 490 nm or emit in the donor to acceptor wavelength range, ruling out any spectroscopic interference.

The initial FRET ratio Q_0 for all samples was the same within 15%. The amplitude from the fit, or relative FRET increase A_1, was averaged for a minimum of two independent assays and plotted against the tetracycline concentration. These data were fit to a modified form of the Hill equation:

$$y = A_{obs,0} - A_{\infty}\frac{[\text{tetracycline}]}{K_{D,app} + [\text{tetracycline}]} \quad (1)$$

where $A_{obs,0}$ is the average amplitude change observed in the absence of tetracycline, A_∞ is the amplitude change for an infinite tetracycline concentration, and $K_{D,app}$ is the apparent dissociation constant for tetracycline.

For measurement of fast kinetics upon addition of high concentrations of *9mer* DNA (no antibiotics), a stopped flow mixing technique based on the Milli-Flow Reactor of the AB2 spectrofluorometer (Thermo Electron Corp.) was employed. *FEH27T* RNA (800 μL) was prepared and annealed at 80 nM (diluted 1:2 in the experiment) in standard buffer as described above. *9mer* DNA was prepared at twice its final concentration in standard buffer, and equal volumes of the two solutions were rapidly mixed in the Milli-Flow Reactor at 25 °C. Excitation was set at 490 nm (8 nm bandwidth), while the tetramethylrhodamine fluorescence emission increase was monitored at 585 nm (16 nm bandwidth). (Monitoring the fluorescein emission decrease at 520 nm yielded rate constants within 20% of those for the tetramethylrhodamine, which is consistent with FRET data where both wavelengths could be monitored simultaneously.) Data at *9mer* concentrations lower than 350 μM were collected with a time resolution of 1 ms, while data at concentrations greater than 350 μM were collected at a resolution of 300 μs. Five to twenty-five time traces were averaged and fit to a single-exponential increase function as described above, yielding rate constants k_{obs} ($=\tau^{-1}$). Error bars (dk) stem from the calculated error in τ_1 (dτ_1) derived from the fit (dk = dτ_1/τ_1^2). The *9mer* concentration dependence of k_{obs} was fit to eq 2 (see the Results) using Levenberg−Marquart least-squares regression implemented in Origin 7.0 (Microcal) to extract the elementary rate constants.

For an independent determination of the *9mer* binding rate constant (k_{on}), *5′FEH27* was prepared at a concentration of 10 nM and annealed in standard buffer as described above for *FEH27T* and additionally degassed prior to measurement by being placed in a Speed-Vac vacufuge for 15 min. The sample (150 μL) was placed in the fluorometer cuvette with excitation at 490 nm (4 nm bandwidth), while emission was monitored at 520 nm (8 nm bandwidth). Given a stable equilibrium fluorescence signal from *5′FEH27*, *9mer* DNA was added to final concentrations of 100 nM to 1 μM, and the resulting kinetic fluorescence increase was fit to a single-exponential increase function as described above. The resulting rate constant ($k_{obs} = \tau_1^{-1}$) was plotted against the *9mer* concentration, and these data were fit by linear regression, where the slope represents the second-order rate constant associated with binding of *9mer* to *5′FEH27*.

RESULTS

NMR Spectroscopy: G890 as a Key Indicator for the 885 and 888 Conformations. Since the base pairing patterns in the proposed H27 conformations are distinct, we determined one-dimensional (1D) imino proton (^{1}H) NMR spectra of three different constructs derived from nucleotides 885−912 in *E. coli* 16S rRNA (Figure 2). Construct *Native* is unmodified; construct *885* carries a U911C mutation to selectively stabilize the 885 conformation; and construct *888* has an extended terminal helix to stabilize the 888 conformation. The secondary structures of the "locked" constructs, *885* and *888*, are identical between bases 895 and 904, and contain a characteristic structural element, a GNRA tetraloop (where N can be any nucleotide, here C, and R is a purine, here A). The imino ^{1}H NMR spectra of the *885* and *888* constructs therefore exhibit several common features (Figure 2A), assigned on the basis of imino−imino and imino−amino nuclear Overhauser effects (NOEs) as well as ^{1}H−^{15}N HSQC spectra (data not shown). The resonance of the first G of the tetraloop appears around 10.6−10.7 ppm, an upfield position consistent with previous GNRA tetraloop studies (*42*, *43*); evidence is observed for three base pairs immediately adjacent to the tetraloop, as indicated by the presence of imino proton resonances corresponding to the G895, G902, and G903 NH1 protons. The G902 and G903 NH1 resonances are observed between 12 and 14 ppm, consistent with Watson−Crick base pairing of these imino protons, while an expected upfield chemical shift to 11.57 ppm is observed for the G895 NH1 resonance involved in the G895·U904 wobble pair. In addition, U904 of this wobble pair shows an expected resonance at 11.77 ppm (Figure 2A).

Notably, the G890 NH1 chemical shift is very different in the *885* and *888* spectra (Figure 2A). In the *888* construct, G890 is predicted to pair with C910, which leads to a G890 NH1 resonance at 12.19 ppm, corresponding to a Watson−Crick base-paired imino proton. In the *885* construct, G890 is predicted to be looped out to form two hydrogen bonds, one each to the adjacent U891 and to a phosphate oxygen on the opposing strand (*8*). The *885* G890 NH1 resonance is found as a relatively broad peak of diminished intensity at 10.21 ppm. This is consistent with NMR spectra of the loop E motif of the sarcin−ricin loop of the large subunit ribosomal RNA, where the corresponding G (G2655 in *E. coli* 23S rRNA and G4319 in rat 28S rRNA) has a nearly identical chemical shift (10.18 ppm) (*44*, *45*). Our findings therefore identify G890 as a key indicator of whether H27 resides in the 885 or 888 conformation.

In the spectrum of the *Native* construct, as expected, ^{1}H NMR resonances are found that correspond to the GNRA tetraloop and the three adjacent base pairs, which are shared among all NMR constructs (Figure 2A). However, we also observe a broad featureless hump, centered around 11 ppm, that is unique to the *Native* construct. In long (∼350 ms) mixing time NOESY spectra, this hump reveals NOEs to Watson−Crick base-paired G and C amino protons, suggesting that it contains G imino proton resonances at the helix terminus partially protected from chemical exchange (data not shown). In addition, we found two different resonances for the G890 NH1 proton, at 10.21 and 12.19 ppm, that are characteristic of the 885 and 888 conformers, respectively (Figure 2A). This observation shows that the

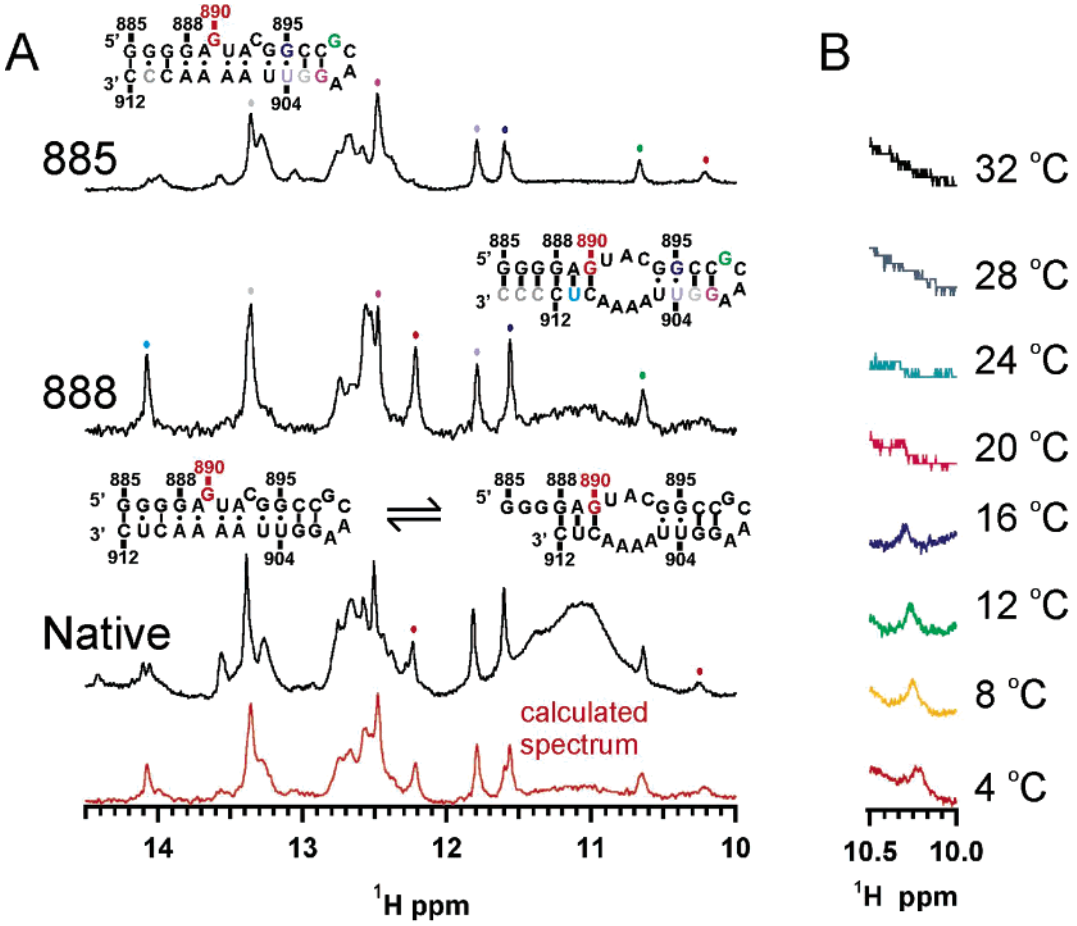

FIGURE 2: 1D imino ^{1}H NMR spectra of three RNA constructs based on *E. coli* H27 in NMR buffer [10 mM Na_iPO_4 (pH 6.4), 0.1 mM EDTA, and 50 mM NaCl], where the color code corresponds to the nucleotide that gives rise to the resonance. (A) Spectra of the *885*, *888*, and *Native* constructs collected at 8 °C. The red spectrum is a linear combination of the spectra of the *885* and *888* constructs, fitted to the spectrum of the *Native* construct. The relative fractions of the 885 and 888 conformations are 0.573 ± 0.04 (f_{885}) and 0.427 ± 0.04 (f_{888}), respectively. (B) A temperature series on the *Native* construct shows that the resonance at ~10.2 ppm, which arises from the G890 imino proton in the 885 conformation, disappears above 20 °C through line broadening, much below the RNA melting temperature (63 °C) and the temperatures at which other resonances are lost (30−50 °C).

Native construct partially occupies both conformations, and that the 885 and 888 conformations either are in slow exchange compared to the NMR time scale or reside in different subpopulations of the RNA. We also performed a temperature series that shows that specifically the resonance at 10.21 ppm, which arises from G890 in the 885 conformation, disappears above 20 °C due to line broadening (Figure 2B), much below the melting temperature of the *Native* construct under these ionic conditions (63 °C, data not shown) and the temperatures at which other resonances are lost (30−50 °C). This is consistent with the previous observation of enhanced conformational dynamics of the bulged G in the loop E motif of 28S rRNA compared to Watson−Crick base pairs (*45*).

To quantify the relative contributions of the 885 and 888 conformations to the *Native* structure, we fit a linear combination of the spectra of the *885* and *888* constructs to the spectrum of the *Native* construct, using the relative contribution of the 888 conformation, f_{888} (where $f_{885} = 1 - f_{888}$), as the only fitting parameter (Materials and Methods) (*46*). An optimized calculated spectrum is found when $f_{888} = 0.427 \pm 0.04$, suggesting that the *Native* construct significantly populates both the 885 and 888 conformations under NMR conditions (Figure 2A).

A Novel UV-Induced Photo-Cross-Link in H27. The 885 conformation of H27 observed in the 30S subunit crystal structures is stabilized by the common loop E motif (*8*, *9*), which often yields a specific intrahelical photo-cross-link upon UV irradiation (*24*). However, in multiple UV irradiation studies of the ribosome, only long-range cross-links involving G894 of H27 and the 5′-domain of 16S rRNA were observed (*47*−*49*). Irradiation of construct *EH27* in standard buffer [chosen to resemble buffer conditions used for kinetic assays of ribosome function (*50*), consisting of 50 mM Tris-HCl (pH 7.5), 50 mM NH_4Cl, and 20 mM $MgCl_2$] at 25 °C with UV light at 254 nm resulted in a major and a minor RNA−RNA photo-cross-link (Figure 3). The major cross-link has a lower gel mobility, accumulates with a single-exponential rate constant of 1.3 h^{-1}, and saturates at ~28% after 2 h. [A minor, slightly higher-mobility cross-link also accumulates single-exponentially, is enhanced by the addition of magnesium, and appears to be located near the 3′-terminus (data not shown).] We purified the major cross-linked species, ^{32}P radiolabeled it on either the 5′- or 3′-end, and analyzed it using alkali and RNase T1 (G-specific) degradation. We thus found that the cross-link covalently couples nucleotides A892 and U905 (Figure 3), which is distinct from

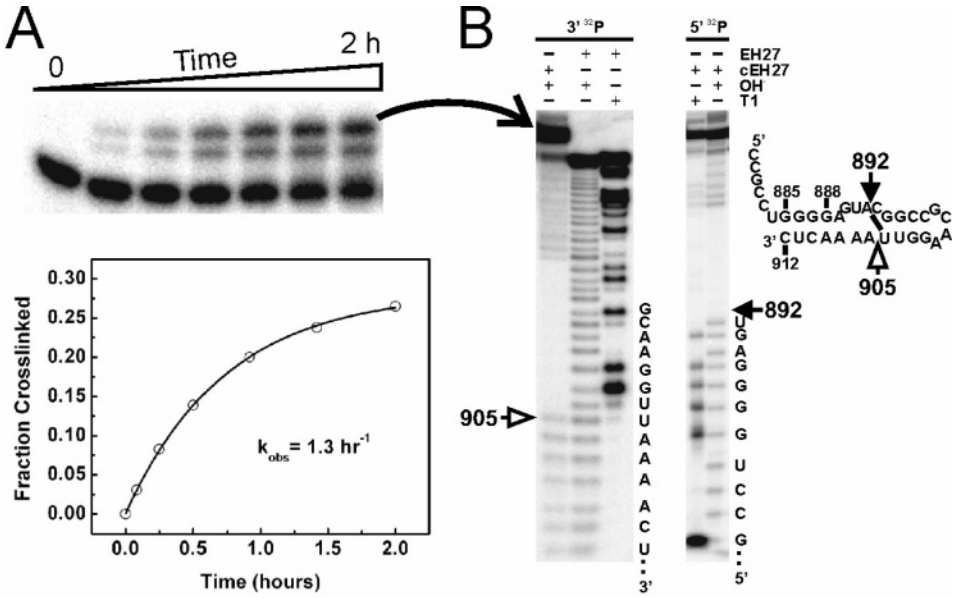

FIGURE 3: Ultraviolet-induced photo-cross-linking of construct *EH27*. (A) Time course of cross-linking. After the samples have been exposed to UV light for only 5 min, two bands of cross-linked RNA are apparent after separation on a denaturing 20% polyacrylamide gel, the uppermost of which grows to ~28% of the total RNA over a 2 h time period with an observed rate constant of 1.3 h^{-1}. (B) Mapping the major cross-linking site. The major (upper) cross-link (termed *cEH27*) was prepared on a large scale and radiolabeled on either the 3′- or 5′-end for comparative analysis on sequencing gels by alkaline hydrolysis (OH^-) and RNase T1 digestion together with the un-cross-linked *EH27*. The cross-link leads to a gap in the alkaline ladder since OH^--induced backbone cleavage 3′ of a nucleotide anywhere between the cross-linked bases will not yield a fragment. Please note that cleavage 3′ of U905 still yields a band in the OH^- lane of the 3′-radiolabeled *cEH27*, while cleavage 3′ of A892 is associated with the first missing fragment in the OH^- lane of the 5′-radiolabeled *cEH27*, thus indicating that the cross-link (dash in the H27 depiction) occurs between nucleotides A892 and U905. Our sequence assignments are indicated beside the sequencing ladders.

the loop E-specific cross-link that is observed between the nucleotides equivalent to U891 and A906 (*24*). Our findings therefore suggest that a structure different from a loop E motif causes the efficient cross-link in H27. Interestingly, neither of the two conformationally "locked" constructs, *885* and *888*, formed a cross-link under the same conditions (data not shown).

Steady-State FRET Demonstrates the Reversibility of Conformational Switching. To more directly test whether the 885 and 888 conformations of H27 interconvert, we designed a FRET-labeled construct *FEH27T*, in which the 5′-end of the *Native* H27 construct is extended by six nucleotides of 16S rRNA sequence, yielding the general sequence denoted *EH27*, while nucleotide modifications at positions 899 and 911 allow fluorophore incorporation to generate the fluorescein- and tetramethylrhodamine-labeled RNA *FEH27T* (Materials and Methods). This design allows for an assay inspired by a previously described DNA-fuelled molecular machine (*51*), in which the partially complementary DNA oligonucleotide *F2* binds to the 5′-overhang as well as adjacent nucleotides 885−887, eliminating the possibility of the RNA assuming the 885 conformation and thereby shifting the population toward the 888 conformation. Such a conformational shift is expected to result in an increase in FRET efficiency between the donor fluorophore (fluorescein) attached to the N of the GNRA tetraloop and the acceptor fluorophore (tetramethylrhodamine) coupled to the base in position 911 (Figure 4). The fluorophore pair is predicted to have a distance of ~42 Å in the 885 conformation of the 30S ribosomal subunit (*8*, *52*), which is close to the fluorophore pair's Förster distance of ~55 Å, making it very sensitive to changes in that distance (*33*). DNA oligonucleotide *F2* contains a 3′-overhang, which allows its removal by addition of the fully complementary DNA oligonucleotide *cF2* to form a long DNA duplex (Figure 4). If conformational switching of *FEH27T* is reversible, this should lead to a decrease in FRET efficiency.

Indeed, when we incubated 20 nM *FEH27T* in standard buffer [50 mM Tris-HCl (pH 7.5), 50 mM NH_4Cl, and 20 mM $MgCl_2$] at 25 °C, we found a relatively low FRET ratio of ~0.36. Upon addition of 100 nM *F2* DNA, we observed an exponential decrease in the donor signal, accompanied by a synchronous increase in the acceptor signal, consistent with an increase in FRET efficiency (Figure 4). After ~800 s, the donor and acceptor signals leveled off at a FRET ratio of ~1.0. Next, we added the fully complementary *cF2* (140 nM), which led to an exponential decrease over ~300 s to a FRET ratio of ~0.42, signifying an essentially complete reversal to the initial FRET ratio (Figure 4). In a control experiment, addition of *cF2* to *FEH27T* in the absence of *F2* resulted in no changes in the FRET ratio, as expected (data not shown). These results provide direct evidence for full reversibility of conformational switching between the 885 and 888 conformations in H27. Furthermore, we noticed a dependence of the kinetics of the FRET increase on the *F2* concentration (data not shown), suggesting that the observed rates report on a bimolecular reaction.

Extracting Fast Rate Constants of Conformational Switching. Our initial observation that the FRET increase as induced by the addition of partially complementary DNA oligonucleotide *F2* exhibits a dependence on the DNA concentration suggests that a bimolecular reaction, rather than unimolecular conformational switching, is rate-limiting. To further test this notion and to ask whether a rate constant for conformational

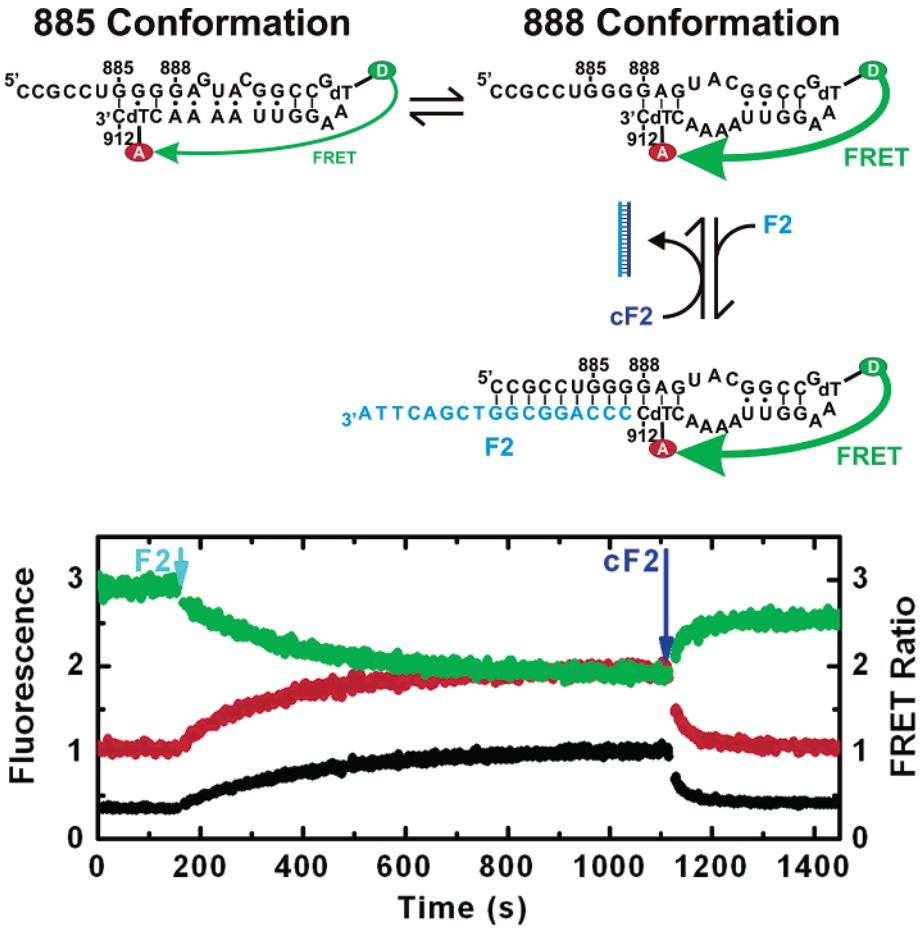

FIGURE 4: Scheme and real-time fluorescence time course of a FRET-monitored "fuel-strand" experiment (*51*), demonstrating reversibility of conformational switching of H27 in standard buffer [50 mM Tris-HCl (pH 7.5), 50 mM NH_4Cl, and 20 mM $MgCl_2$] at 25 °C. Construct *FEH27T* is doubly labeled with donor (fluorescein, green) and acceptor (tetramethylrhodamine, red) fluorophores. Upon addition of the partially complementary DNA oligonucleotide *F2* (indicated in cyan), the donor emission decreases, while the acceptor emission and the resulting FRET ratio (black) increase, as expected from a shift from the 885 conformation to the 888 conformation. Upon addition of DNA oligonucleotide *cF2* (indicated in blue), which forms a DNA duplex with *F2* and thus removes it from *FEH27T*, the FRET ratio decreases back to its initial value.

switching can be extracted at saturating DNA concentrations, we performed a DNA titration experiment. We utilized a DNA oligonucleotide, termed *9mer*, that binds to the same region (residues 879−887) of *FEH27T* as *F2*, but lacks its 3′-overhang. A representative stopped-flow time course of the acceptor fluorescence signal (representative of the increase in the rate of FRET; the donor fluorescence decreased with similar kinetics), measured at 1.8 mM *9mer*, is shown in Figure 5A. The signal increase was >30% and was complete less than 100 ms after DNA addition. The data were fit with a single-exponential increase function, yielding a rate constant of $84 \pm 3\ s^{-1}$. By performing this experiment over a broad range (from 2 μM to 1.8 mM) of *9mer* concentrations, we obtained the titration curve shown in Figure 5B.

The rate constants observed for the induced change in acceptor fluorescence are linearly dependent on the *9mer* DNA concentration up to ~900 μM. At *9mer* concentrations of >1 mM, a deviation from this linear dependence was observed (Figure 5B), indicative of the beginning of *9mer* saturation as unimolecular conformational switching becomes rate-limiting (which is independent of *9mer* concentration, predicting a flat line). To extract rate constants for conformational switching, we considered the following reaction mechanism similar to the one shown in Figure 4:

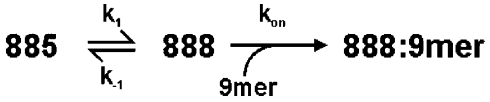

This minimal reaction scheme is based on the fact that we have evidence for reversible switching between the 885 and 888 conformations (with rate constants k_1 and k_{-1}) through our "fuel-strand" experiment of Figure 4. In addition, it assumes that *9mer* binding captures and traps H27 in the high-FRET 888 conformation to form the 888−*9mer* complex, thus generating the observed FRET increase. This mechanism leads to the following analytical expression for k_{obs}:

$$k_{obs} = \frac{k_1 k_{on}[9mer]}{k_1 + k_{-1} + k_{on}[9mer]} \qquad (2)$$

To reduce the number of variables in our fit, an independent determination of the *9mer* binding rate constant k_{on} is necessary. To this end, the initially unlabeled RNA *EH27* (identical in sequence to *FEH27T*) was enzymatically 5′-phosphorothioated and then labeled with fluorescein-5-maleimide to yield *5′FEH27* (Materials and Methods). The

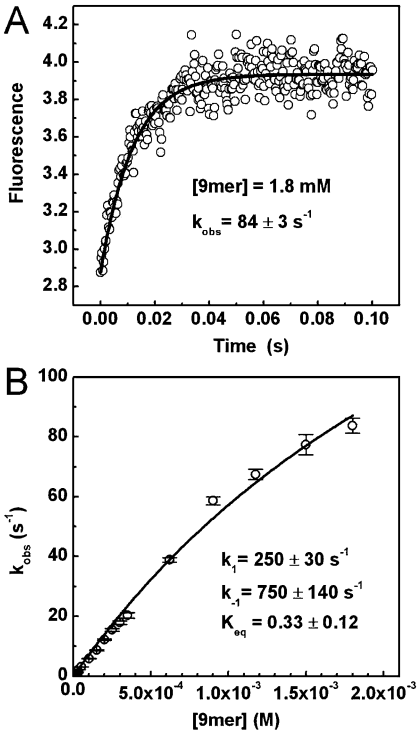

FIGURE 5: Stopped-flow kinetics monitoring the acceptor fluorescence increase in standard buffer [50 mM Tris-HCl (pH 7.5), 50 mM NH_4Cl, and 20 mM $MgCl_2$] at 25 °C upon addition of *9mer* at different concentrations to shift the FRET-labeled *FEH27T* construct into the 888 conformation. (A) Fluorescence emission at 585 nm with excitation at 490 nm, averaged over 14 individual stopped-flow time traces collected upon addition of 1.8 mM *9mer* (○). Single-exponential fit yielding a k_{obs} of 84 ± 3 s^{-1} (—). (B) Plot of k_{obs} derived from data sets as in panel A, collected over a range of *9mer* concentrations. Fit to eq 2 based on kinetic Scheme 1, yielding values for the forward and reverse rate constants, k_1 and k_{-1}, respectively, which characterize the rapid exchange between the 885 and 888 conformers (—).

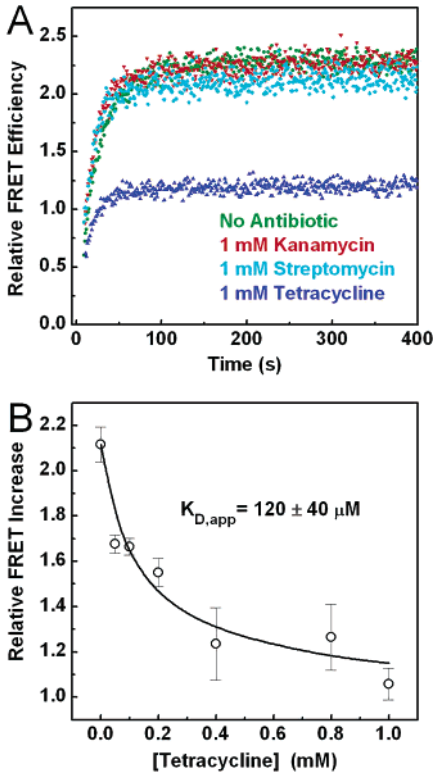

FIGURE 6: Effects of streptomycin, kanamycin, and tetracycline on the *9mer*-induced shift of the FRET-labeled construct *FEH27T* to the 888 conformation in 300 mM Tris-HCl (pH 7.5), 50 mM NH_4Cl, and 20 mM $MgCl_2$ at 25 °C. (A) Plot of the relative FRET efficiency recorded after the addition of 400 nM *9mer* DNA to *FEH27T* in the presence of 1 mM tetracycline, streptomycin, or kanamycin as indicated. (B) Plot of the change in the relative FRET efficiency upon addition of 400 nM *9mer* in the presence of increasing concentrations of tetracycline. Fit of the data to a modified form of the Hill equation (eq 1) to derive an apparent dissociation constant for tetracycline, $K_{D,app}$ (—).

5′-fluorescein label of this construct responds to the adjacent binding of *9mer* through nucleotide-specific fluorescence dequenching (*53*), independent of conformational switching. As expected, the observed rate constant of the fluorescence decrease upon addition of *9mer* DNA was linearly dependent on the *9mer* concentration; the slope of this linear dependence yielded the rate constant for binding of *9mer* to *FEH27* as previously described (*53*) [k_{on} = (2.96 ± 0.45) × 10^5 M^{-1} s^{-1} (data not shown)]. Using this independently derived value for k_{on}, the resulting fit of eq 2 to the titration data in Figure 5B yielded a k_1 of 250 ± 30 s^{-1} and a k_{-1} of 750 ± 150 s^{-1} for conformational switching under standard conditions [50 mM Tris-HCl (pH 7.5), 50 mM NH_4Cl, and 20 mM $MgCl_2$, at 25 °C]. The equilibrium constant between the 888 and 885 conformations ([888]/[885] = k_1/k_{-1}) is therefore 0.33 ± 0.12.

Tetracycline Inhibits Conformational Switching. Tetracycline is known to bind to the 30S ribosomal subunit close to A892 of H27 (*54*, *55*). To ask whether tetracycline may specifically interfere with conformational switching of H27, we studied the effects of tetracycline and, as controls, the aminoglycoside antibiotics streptomycin and kanamycin on the *9mer*-induced conformational shift of the FRET-labeled construct *FEH27T* into the 888 conformation. As shown in Figure 6A, addition of neither 1 mM streptomycin nor kanamycin has any impact on the observed FRET change upon *9mer* addition. By contrast, in the presence of 1 mM tetracycline, an ~50% decrease in the relative change in FRET efficiency is observed. We performed similar experiments in the presence of increasing concentrations of tetracycline, leading to a hyperbolic decrease in the relative FRET change, which yielded an apparent dissociation constant for tetracycline of 120 ± 40 μM (Figure 6B).

DISCUSSION

The diverse functions of RNA in storage, processing, and regulation of genetic information derive from its structural diversity. RNA can form long straight helices when storing genetic information of a virus, or assume a fold as intricate as a ribosomal particle when performing a tightly controlled catalytic task. The limited four-letter alphabet of RNA allows for a multitude of (nearly) isoenergetic alternative structures, which can interconvert as required for a specific task such as the translational cycle. This is perhaps the main reason the ribosome was conserved up to the present as an RNA-based enzyme after it enabled the template-directed synthesis of peptides and protein enzymes in a prebiotic RNA world (*10*, *56*).

The kinetics and thermodynamics of interconversion of alternative folds of an RNA determine its functional performance. NMR studies and MD simulations suggest that individual base pair lifetimes are in the millisecond time

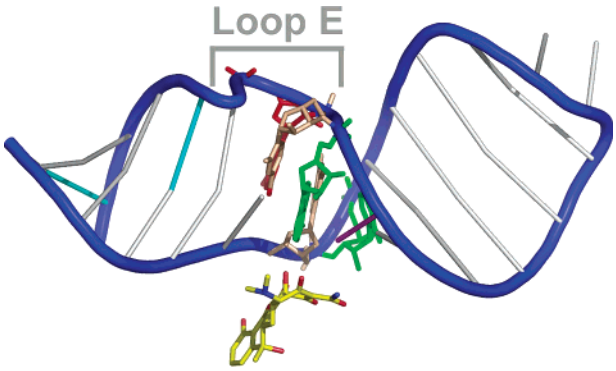

FIGURE 7: H27 from *E. coli* 16 rRNA with bound tetracycline (PDB entry 1HNW) (*54*). Nucleotides 885 and 888 are colored cyan, and the looped out G890, part of loop E which produces a key resonance in our NMR studies, is colored red. A cross-link characteristic of loop E involves U891 and A906 (tan), whereas the cross-link observed in our studies of the isolated H27 occurs between A892 and U905 (both green). In the crystal structure, tetracycline (yellow) interacts with nucleotides A892 and C893 (magenta stick). This figure was constructed with Nuccyl and rendered with MacPyMOL.

range (*25*, *26*), while a full ribosomal cycle probably takes several tens to hundreds of milliseconds (*57*, *58*), suggesting that individual structural rearrangements in the ribosome must occur on the intermediate time scale. Here we have used a combination of 1D ^{1}H NMR spectroscopy, UV-induced photo-cross-linking, and fluorescence spectroscopy to acquire a kinetic and thermodynamic framework for a possible conformational rearrangement in the slippery sequence of H27 from *E. coli* 16S rRNA using model systems identical in sequence. We find a specific NMR resonance (that of the imino proton of G890, which in the 885 conformation is looped out in a loop E motif but in the 888 conformation is involved in a Watson−Crick base pair) to be a key indicator for the presence of the 885 and 888 conformations. Both the 885 and 888 conformations are highly populated in the isolated H27 under NMR conditions, with a slight, 57%-over-43% excess of the 885 conformation (Figure 2). UV irradiation produces an efficient intramolecular photo-cross-link between nucleotides 892 and 905 that is distinct from a cross-link between nucleotides 891 and 906 expected for a loop E motif (Figures 3 and 7). Taken together with the fact that neither of the two locked conformers cross-links, these findings further support the notion that the isolated H27 coexists in multiple conformations. While these observations do not provide direct evidence for an exchange between conformations, fluorescence resonance energy transfer (FRET) shows that addition of a partially complementary DNA oligonucleotide rapidly shifts the 885 to the 888 conformation, revealing an elementary rate constant for the forward reaction of ~250 s^{-1} under conditions adapted from assays of ribosomal function (Figures 4 and 5). The reversal is 3-fold as fast, thus thermodynamically favoring the 885 conformation over the 888 conformation, possibly due to the stabilizing effect of the loop E motif. Finally, the antibiotic tetracycline, known to bind to the 885 conformation of H27 in the ribosomal crystal structures (*54*, *55*) (Figure 7), suppresses the induced shift to the 888 conformation with a concentration dependence yielding an apparent dissociation constant of 120 μM. This is consistent with a stabilizing thermodynamic effect of tetracycline on the 885 conformation.

Surprisingly Rapid Exchange Kinetics of a Slippery Sequence. The rate constants we estimate for the reversible interconversion of the 885 and 888 conformers of H27, 250 and 750 s^{-1}, are only somewhat slower than the opening rates of individual base pairs, depending on their nature and position in an RNA duplex. For example, nonterminal G·C base pairs were found to open to an extent sufficient for imino proton exchange with the solvent at rate constants of ~20−400 s^{-1}, whereas nonterminal A·U base pairs have estimated opening rate constants faster than 10 000 s^{-1} (*25*). End fraying often leads to additional acceleration of the opening of terminal base pairs (*59*). The fact that the reversible 885-to-888 conformational change, entailing a three-base pair slippage (Figure 1C), can occur surprisingly rapidly compared to opening of a single base pair suggests that slippage is mechanistically not much more challenging than a simple base pair opening. Interestingly, little is known about the underlying molecular mechanism of slippage, despite the fact that it contributes significantly to biologically important processes such as DNA mutagenesis and evolution of genomes (*60*) as well as ribosomal frameshifting (*27*). Our results suggest that the opening of (or at least partial loss of hydrogen bonding in) a single base pair such as a G887·C910 base pair in the 885 conformer (Figure 1C) may be the starting point for slippage. The adjacent G888·A909 noncanonical pair would have to open concomitantly to accommodate the first new pairing, G888·C910, followed by rapid adjustments forming G887·U911 and G886·C912 base pairs. Similar sliding must happen twice more until the 888 conformation with its G888·C912 base pair is reached, offering a mechanism with a low energy barrier because few hydrogen bonds are broken at any given time. One of the multiple conformational intermediates of such a sequential sliding mechanism may then lead to efficient cross-linking of nucleotides A892 and U905, which are nearly 8 Å apart and separated by an unpaired C893 in the 885 conformation of the ribosomal crystal structures (Figure 7) (*8*). The latter notion is further corroborated by the fact that we do not find evidence in the NMR spectra of any of our three H27 constructs for involvement of U905 in a G894·U905 base pair (Figure 2), which is consistent with this cross-linked base being dynamic.

The proposed mechanism for H27 conformational exchange is likely analogous to the essential rearrangement observed in the substrate domain of the VS ribozyme, where a series of adjacent guanines also facilitates slippage (*28*, *61*). A related exchange between frayed base pairs has been proposed as a mechanism for branch migration in DNA recombination events (*62*, *63*). As may be expected, the topologically more challenging branch migration between four DNA strands proceeds with a rate constant of ~35 s^{-1} (*62*), roughly 1 order of magnitude slower than our conformational exchange in H27 from 16S rRNA. Crothers and co-workers previously studied a large structural rearrangement involving branch migration in the spliced leader (SL) RNA from *Leptomonas collosoma* (*64*). In an approach similar to that employed here, the authors used partially complementary DNA oligonucleotides to specifically shift the secondary structure of SL RNA toward one of its two nearly isoenergetic conformations. Consistent with the larger scale of rearrangements in SL RNA compared to H27, the authors estimated an interconversion rate constant of ~7 s^{-1}

(*64*), ~2 orders of magnitude slower than that for H27 conformational exchange.

Thermodynamics Slightly Favors the 885 Conformation. Using the nearest-neighbor free energy parameters of Zuker and Turner (*65*, *66*), the 888 conformer of H27 is computationally predicted to be 2.5 kcal/mol more stable than the 885 conformer (−8.9 vs −6.4 kcal/mol). By contrast, the 888−885 equilibrium constant derived from our FRET experiments is 0.33; that is, it slightly favors the 885 conformation by ~0.7 kcal/mol. Certainly, differences in conditions (1 M NaCl at 37 °C for the computational prediction, 50 mM NH_4Cl and 20 mM $MgCl_2$ at 25 °C in our experimental studies) may contribute to this discrepancy, especially since under NMR conditions (50 mM NaCl at 8 °C) we find a 0.427:0.573 (=0.75) intermediate 888:885 distribution. However, the computational algorithm does not account for the extended noncanonical base pairs in the loop E motif of the 885 conformation and in fact adds a penalty to the energy calculation for the larger "internal loop" represented by this motif (*65*). Of course, the 888 conformation will also likely contain noncanonical base pairs (for which we cannot account), which will partially counter the imbalance in the calculation. But it is also tempting to speculate that perhaps the 885 conformation's loop E motif is a particularly stable structure that slightly stabilizes the 885 conformation over the 888 conformation, as we observe experimentally.

There is reason to believe that the loop E motif may be a particularly stable structural element. Loop E has been recognized as a widespread organizing motif in the ribosomal RNAs as well as the hairpin ribozyme (*24*). It is, when isolated from the ribosomal matrix, conducive to NMR spectroscopic (*44*) and X-ray crystallographic structure determination (*67*) as well as thermodynamic measurements (*68*), and is reported to remain stable in extended molecular dynamics simulations (*69*, *70*). Interestingly, we find it to be thermodynamically stabilized even further by tetracycline binding, which may be explained by the crystallographically observed interaction with A892 and C893 in the 885 conformation of H27 (Figure 7) (*54*, *55*). Nevertheless, the 885 and 888 conformations are still close to isoenergetic, suggesting that yet unknown noncanonical base pairs must be stabilizing the 888 conformation as well.

Structural and Functional Context of H27 in the Ribosome. In all crystal structures of the 30S ribosomal subunit, the minor groove of the H27 loop E motif closely packs against H44 of the 3′-terminal domain, which harbors the decoding center in 16S rRNA. Additionally, two bases adjacent to H27 loop E, C893 and G894, make hydrogen bonding and stacking interactions, respectively, with U244 from H11 of the 5′-domain (*8*). It is plausible that these interactions within the ribosomal matrix further stabilize the 885 conformation over the 888 conformation, both thermodynamically and kinetically. A particular boost to the original switch helix hypothesis that proposed cycling of H27 between the 885 and 888 conformations during translation (*19*, *20*) came from the fact that in all crystal structures H27 knits together distant parts of 16S rRNA, particularly the decoding center in H44 with H11 of the 5′-domain. Once the message has been decoded, H27 then could plausibly transduce local dynamics into the global structural rearrangements observed by cryo-electron microscopy (*3*−*7*). If indeed no H27 conformational cycling occurs in present day ribosomes, which is the current belief (*12*, *23*), it is intriguing to ask how tertiary structure contacts in the ribosomal matrix may so completely suppress the inherent dynamics we observe for the two nearly isoenergetic conformations of an isolated H27. Given the high degree of evolutionary conservation of the H27 sequence (*14*), one may speculate that perhaps a prebiotic RNA-only ribosome relied on conformational switching. Yet when translocation became catalyzed by an EF-G-like protein cofactor, more subtle conformational adjustments around H27 began to suffice, especially in a region that overall appears to be very dynamic (*6*, *71*). Such subtle adjustments may involve, for example, only partial slippage by one or two, rather than all three, nucleotides of the full 885-to-888 conformational switch.

Suppression of conformational adjustments around H27 may also present another mode of action for the broad-spectrum antibiotic tetracycline that primarily seems to inhibit translation by blocking binding of aminoacylated tRNA to the ribosomal A-site. Two independent atomic-resolution crystal structures of *Thermus thermophilus* 30S subunits in complex with tetracycline revealed multiple binding sites for the antibiotic (*54*, *55*). A primary binding site is located near H34 in the 30S A-site, which is in agreement with previous biochemical studies as well as cryo-EM localization of the Tet(O) protection protein (*72*, *73*). Tetracycline also inserts between H27 and H11 to bind to A892 and C893, becoming the secondary binding site with a slightly lower occupancy relative to the primary binding site when 80 μM tetracycline is soaked into 30S crystals (*54*) (Figure 7). This secondary site is also observed in the ribosome upon addition of 120 μM tetracycline through the protection of A892 from DMS modification (*72*) and a direct UV cross-link between G890 and the antibiotic (*74*). Strikingly, our apparent tetracycline dissociation constant of 120 μM based on suppression of H27 conformational dynamics matches the concentration range where it appears to bind to H27 in the ribosome. Clearly, tetracycline is promiscuous in its binding to RNA since four additional binding sites are partially occupied in one of the two 30S crystal structures (*55*), and it has been observed to inhibit catalysis in both the hammerhead and hepatitis delta virus ribozymes (*75*, *76*). However, the apparent dissociation constants are markedly reduced (to ~500 μM) in the latter cases, suggesting that the tetracycline effect we observe for H27 is quite specific. Thus, while the ribosome may no longer fully exploit the rapid conformational dynamics inherent to a slippery sequence such as that of H27 from *E. coli* 16S rRNA, a broad-spectrum antibiotic such as tetracycline still specifically targets H27, presumably to inhibit translation. We are only starting to glimpse the complex linkage between local and global structural rearrangements in the ribosomal machinery during protein biosynthesis, yet it is clear that model systems such as H27 will help bridge our current gap in understanding.

ACKNOWLEDGMENT

We thank all members of the Walter lab for helpful discussions and especially Dr. David Rueda for his help in constructing the calculated spectrum of Figure 2. We are grateful to Eric Watt, Matthew Revington, and Professors Hashim Al-Hashimi, Erik Zuiderweg, and Ronald Micura for assistance with collection and processing of NMR spectra.

We also thank Professors Bruce Palfey and Carol Fierke for helpful discussions about the treatment of kinetic data.

REFERENCES

1. Frank, J. (2002) Single-particle imaging of macromolecules by cryo-electron microscopy, *Annu. Rev. Biophys. Biomol. Struct. 31*, 303−319.
2. Rodnina, M. V., Daviter, T., Gromadski, K., and Wintermeyer, W. (2002) Structural dynamics of ribosomal RNA during decoding on the ribosome, *Biochimie 84*, 745−754.
3. Frank, J., and Agrawal, R. K. (2000) A ratchet-like inter-subunit reorganization of the ribosome during translocation, *Nature 406*, 318−322.
4. Gao, H., Sengupta, J., Valle, M., Korostelev, A., Eswar, N., Stagg, S. M., Van Roey, P., Agrawal, R. K., Harvey, S. C., Sali, A., Chapman, M. S., and Frank, J. (2003) Study of the structural dynamics of the *E. coli* 70S ribosome using real-space refinement, *Cell 113*, 789−801.
5. Valle, M., Zavialov, A., Sengupta, J., Rawat, U., Ehrenberg, M., and Frank, J. (2003) Locking and unlocking of ribosomal motions, *Cell 114*, 123−134.
6. Tama, F., Valle, M., Frank, J., and Brooks, C. L., III (2003) Dynamic reorganization of the functionally active ribosome explored by normal mode analysis and cryo-electron microscopy, *Proc. Natl. Acad. Sci. U.S.A. 100*, 9319−9323.
7. Savelsbergh, A., Katunin, V. I., Mohr, D., Peske, F., Rodnina, M. V., and Wintermeyer, W. (2003) An elongation factor G-induced ribosome rearrangement precedes tRNA-mRNA translocation, *Mol. Cell 11*, 1517−1523.
8. Wimberly, B. T., Brodersen, D. E., Clemons, W. M., Jr., Morgan-Warren, R. J., Carter, A. P., Vonrhein, C., Hartsch, T., and Ramakrishnan, V. (2000) Structure of the 30S ribosomal subunit, *Nature 407*, 327−339.
9. Schluenzen, F., Tocilj, A., Zarivach, R., Harms, J., Gluehmann, M., Janell, D., Bashan, A., Bartels, H., Agmon, I., Franceschi, F., and Yonath, A. (2000) Structure of functionally activated small ribosomal subunit at 3.3 Å resolution, *Cell 102*, 615−623.
10. Ban, N., Nissen, P., Hansen, J., Moore, P. B., and Steitz, T. A. (2000) The complete atomic structure of the large ribosomal subunit at 2.4 Å resolution, *Science 289*, 905−920.
11. Ogle, J. M., Murphy, F. V., Tarry, M. J., and Ramakrishnan, V. (2002) Selection of tRNA by the ribosome requires a transition from an open to a closed form, *Cell 111*, 721−732.
12. Ogle, J. M., Carter, A. P., and Ramakrishnan, V. (2003) Insights into the decoding mechanism from recent ribosome structures, *Trends Biochem. Sci. 28*, 259−266.
13. Yusupov, M. M., Yusupova, G. Z., Baucom, A., Lieberman, K., Earnest, T. N., Cate, J. H., and Noller, H. F. (2001) Crystal structure of the ribosome at 5.5 Å resolution, *Science 292*, 883−896.
14. Woese, C. R., Gutell, R., Gupta, R., and Noller, H. F. (1983) Detailed analysis of the higher-order structure of 16S-like ribosomal ribonucleic acids, *Microbiol. Rev. 47*, 621−669.
15. Gutell, R. R., Larsen, N., and Woese, C. R. (1994) Lessons from an evolving rRNA: 16S and 23S rRNA structures from a comparative perspective, *Microbiol. Rev. 58*, 10−26.
16. Montandon, P. E., Wagner, R., and Stutz, E. (1986) *E. coli* ribosomes with a C912 to U base change in the 16S rRNA are streptomycin resistant, *EMBO J. 5*, 3705−3708.
17. Frattali, A. L., Flynn, M. K., De Stasio, E. A., and Dahlberg, A. E. (1990) Effects of mutagenesis of C912 in the streptomycin binding region of *Escherichia coli* 16S ribosomal RNA, *Biochim. Biophys. Acta 1050*, 27−33.
18. Lodmell, J. S., Gutell, R. R., and Dahlberg, A. E. (1995) Genetic and comparative analyses reveal an alternative secondary structure in the region of nt 912 of *Escherichia coli* 16S rRNA, *Proc. Natl. Acad. Sci. U.S.A. 92*, 10555−10559.
19. Lodmell, J. S., and Dahlberg, A. E. (1997) A conformational switch in *Escherichia coli* 16S ribosomal RNA during decoding of messenger RNA, *Science 277*, 1262−1267.
20. Gabashvili, I. S., Agrawal, R. K., Grassucci, R., Squires, C. L., Dahlberg, A. E., and Frank, J. (1999) Major rearrangements in the 70S ribosomal 3D structure caused by a conformational switch in 16S ribosomal RNA, *EMBO J. 18*, 6501−6507.
21. Ogle, J. M., Broderson, D. E., Clemons, W. M., Jr., Tarray, M. J., Carter, A. P., and Ramakrishnan, V. (2001) Recognition of cognate transfer RNA by the 30S ribosomal subunit, *Science 292*, 897−902.
22. Vila-Sanjurjo, A., Ridgeway, W. K., Seymaner, V., Zhang, W., Santoso, S., Yu, K., and Cate, J. H. (2003) X-ray crystal structures of the WT and a hyper-accurate ribosome from *Escherichia coli*, *Proc. Natl. Acad. Sci. U.S.A. 100*, 8682−8687.
23. Rodriguez-Correa, D., and Dahlberg, A. E. (2004) Genetic evidence against the 16S ribosomal RNA helix 27 conformational switch model, *RNA 10*, 28−33.
24. Leontis, N. B., and Westhof, E. (1998) A common motif organizes the structure of multi-helix loops in 16 and 23S ribosomal RNAs, *J. Mol. Biol. 283*, 571−583.
25. Snoussi, K., and Leroy, J. L. (2001) Imino proton exchange and base-pair kinetics in RNA duplexes, *Biochemistry 40*, 8898−8904.
26. Pan, Y., and MacKerell, A. D., Jr. (2003) Altered structural fluctuations in duplex RNA versus DNA: a conformational switch involving base pair opening, *Nucleic Acids Res. 31*, 7131−7140.
27. Namy, O., Rousset, J. P., Naphthine, S., and Brierley, I. (2004) Reprogrammed genetic decoding in cellular gene expression, *Mol. Cell 13*, 157−168.
28. Zamel, R., and Collins, R. A. (2002) Rearrangement of substrate secondary structure facilitates binding to the *Neurospora* VS ribozyme, *J. Mol. Biol. 324*, 903−915.
29. Recht, M. I., and Williamson, J. R. (2001) Central domain assembly: thermodynamics and kinetics of S6 and S18 binding to an S15−RNA complex, *J. Mol. Biol. 313*, 35−48.
30. Lynch, S. R., Gonzalez, R. L., and Puglisi, J. D. (2003) Comparison of X-ray crystal structure of the 30S subunit-antibiotic complex with NMR structure of decoding site oligonucleotide-paromomycin complex, *Structure 11*, 43−53.
31. Goody, T. A., Melcher, S. E., Norman, D. G., and Lilley, D. M. (2004) The kink-turn motif in RNA is dimorphic, and metal ion-dependent, *RNA 10*, 254−264.
32. He, B., Rong, M., Lyakhov, D., Gartenstein, H., Diaz, G., Castagna, R., McAllister, W. T., and Durbin, R. K. (1997) Rapid mutagenesis and purification of phage RNA polymerases, *Protein Expression Purif. 9*, 142−151.
33. Walter, N. G. (2001) Structural dynamics of catalytic RNA highlighted by fluorescence resonance energy transfer, *Methods 25*, 19−30.
34. Walter, N. G. (2002) in *Current Protocols in Nucleic Acid Chemistry*, pp 11.10.1−11.10.23, Wiley, New York.
35. Czworkowski, J., Odom, O. W., and Hardesty, B. (1991) Fluorescence study of the topology of messenger RNA bound to the 30S ribosomal subunit of *Escherichia coli*, *Biochemistry 30*, 4821−4830.
36. Grzesiek, S., and Bax, A. (1993) Measurement of amide proton exchange rates and NOEs with water in $^{13}C/^{15}N$-enriched calcineurin B, *J. Biomol. NMR 3*, 627−638.
37. Piotto, M., Saudek, V., and Sklenar, V. (1992) Gradient-tailored excitation for single-quantum NMR spectroscopy of aqueous solutions, *J. Biomol. NMR 2*, 661−665.
38. Marion, D., Driscoll, P. C., Kay, L. E., Wingfield, P. T., Bax, A., Gronenborn, A. M., and Clore, G. M. (1989) Overcoming the overlap problem in the assignment of ^{1}H NMR spectra of larger proteins by use of three-dimensional heteronuclear ^{1}H-^{15}N Hartmann−Hahn-multiple quantum coherence and nuclear Overhauser-multiple quantum coherence spectroscopy: application to interleukin 1β, *Biochemistry 28*, 6150−6156.
39. Delaglio, F., Grzesiek, S., Vuister, G. W., Zhu, G., Pfeifer, J., and Bax, A. (1995) NMRPipe: a multidimensional spectral processing system based on UNIX pipes, *J. Biomol. NMR 6*, 277−293.
40. Jeong, S., Sefcikova, J., Tinsley, R. A., Rueda, D., and Walter, N. G. (2003) Trans-acting hepatitis delta virus ribozyme: catalytic core and global structure are dependent on the 5′ substrate sequence, *Biochemistry 42*, 7727−7740.
41. Pereira, M. B., Harris, D. A., Rueda, D., and Walter, N. G. (2002)- The reaction pathway of the trans-acting hepatitis delta virus ribozyme: a conformational change accompanies catalysis, *Biochemistry 41*, 730−740.
42. Heus, H. A., and Pardi, A. (1991) Structural features that give rise to the unusual stability of RNA hairpins containing GNRA loops, *Science 253*, 191−194.
43. Jucker, F. M., Heus, H. A., Yip, P. F., Moors, E. H., and Pardi, A. (1996) A network of heterogeneous hydrogen bonds in GNRA tetraloops, *J. Mol. Biol. 264*, 968−980.

44. Szewczak, A. A., and Moore, P. B. (1995) The sarcin/ricin loop, a modular RNA, *J. Mol. Biol. 247*, 81−98.
45. Seggerson, K., and Moore, P. B. (1998) Structure and stability of variants of the sarcin-ricin loop of 28S rRNA: NMR studies of the prokaryotic SRL and a functional mutant, *RNA 4*, 1203−1215.
46. Hobartner, C., and Micura, R. (2003) Bistable secondary structures of small RNAs and their structural probing by comparative imino proton NMR spectroscopy, *J. Mol. Biol. 325*, 421−431.
47. Wilms, C., Noah, J. W., Zhong, D., and Wollenzien, P. (1997) Exact determination of UV-induced crosslinks in 16S ribosomal RNA in 30S ribosomal subunits, *RNA 3*, 602−612.
48. Noah, J. W., Shapkina, T., and Wollenzien, P. (2000) UV-induced cross-links in the 16S rRNAs of *Escherichia coli*, *Bacillus subtilis* and *Thermus aquaticus* and their implications for ribosome structure and photochemistry, *Nucleic Acids Res. 28*, 3785−3792.
49. Shapkina, T., Lappi, S., Franzen, S., and Wollenzien, P. (2004) Efficiency and pattern of UV pulse laser-induced RNA-RNA cross-linking in the ribosome, *Nucleic Acids Res. 32*, 1518−1526.
50. Pape, T., Wintermeyer, W., and Rodnina, M. V. (1998) Complete kinetic mechanism of elongation factor Tu-dependent binding of aminoacyl-tRNA to the A site of the *E. coli* ribosome, *EMBO J. 17*, 7490−7497.
51. Yurke, B., Turberfield, A. J., Mills, A. P., Jr., Simmel, F. C., and Neumann, J. L. (2000) A DNA-fuelled molecular machine made of DNA, *Nature 406*, 605−608.
52. Tung, C. S., Joseph, S., and Sanbonmatsu, K. Y. (2002) All-atom homology model of the *Escherichia coli* 30S ribosomal subunit, *Nat. Struct. Biol. 9*, 750−755.
53. Walter, N. G., and Burke, J. M. (1997) Real-time monitoring of hairpin ribozyme kinetics through base-specific quenching of fluorescein-labeled substrates, *RNA 3*, 392−404.
54. Brodersen, D. E., Clemons, W. M., Jr., Carter, A. P., Morgan-Warren, R. J., Wimberly, B. T., and Ramakrishnan, V. (2000) The structural basis for the action of the antibiotics tetracycline, pactamycin, and hygromycin B on the 30S ribosomal subunit, *Cell 103*, 1143−1154.
55. Pioletti, M., Schlunzen, F., Harms, J., Zarivach, R., Gluhmann, M., Avila, H., Bashan, A., Bartels, H., Auerbach, T., Jacobi, C., Hartsch, T., Yonath, A., and Franceschi, F. (2001) Crystal structures of complexes of the small ribosomal subunit with tetracycline, edeine and IF3, *EMBO J. 20*, 1829−1839.
56. Gesteland, R. F., Cech, T. R., and Atkins, J. F. E. (1999) *The RNA World*, 2nd ed., Cold Spring Harbor Laboratory Press, Plainview, NY.
57. Katunin, V. I., Muth, G. W., Strobel, S. A., Wintermeyer, W., and Rodnina, M. V. (2002) Important contribution to catalysis of peptide bond formation by a single ionizing group within the ribosome, *Mol. Cell 10*, 339−346.
58. Youngman, E. M., Brunelle, J. L., Kochaniak, A. B., and Green, R. (2004) The active site of the ribosome is composed of two layers of conserved nucleotides with distinct roles in peptide bond formation and peptide release, *Cell 117*, 589−599.
59. Fritzsche, H., Kan, L. S., and Ts'o, P. O. (1983) Nuclear magnetic resonance study on the exchange behavior of the NH−N protons of a ribonucleic acid miniduplex, *Biochemistry 22*, 277−280.
60. Lovett, S. T. (2004) Encoded errors: mutations and rearrangements mediated by misalignment at repetitive DNA sequences, *Mol. Microbiol. 52*, 1243−1253.
61. Hoffmann, B., Mitchell, G. T., Gendron, P., Major, F., Andersen, A. A., Collins, R. A., and Legault, P. (2003) NMR structure of the active conformation of the Varkud satellite ribozyme cleavage site, *Proc. Natl. Acad. Sci. U.S.A. 100*, 7003−7008.
62. Mulrooney, S. B., Fishel, R. A., Hejna, J. A., and Warner, R. C. (1996) Preparation of figure 8 and cruciform DNAs and their use in studies of the kinetics of branch migration, *J. Biol. Chem. 271*, 9648−9659.
63. Yamada, K., Ariyoshi, M., and Morikawa, K. (2004) Three-dimensional structural views of branch migration and resolution in DNA homologous recombination, *Curr. Opin. Struct. Biol. 14*, 130−137.
64. LeCuyer, K. A., and Crothers, D. M. (1994) Kinetics of an RNA conformational switch, *Proc. Natl. Acad. Sci. U.S.A. 91*, 3373−3377.
65. Mathews, D. H., Sabina, J., Zuker, M., and Turner, D. H. (1999) Expanded sequence dependence of thermodynamic parameters improves prediction of RNA secondary structure, *J. Mol. Biol. 288*, 911−940.
66. Zuker, M. (2003) Mfold web server for nucleic acid folding and hybridization prediction, *Nucleic Acids Res. 31*, 3406−3415.
67. Correll, C. C., Freeborn, B., Moore, P. B., and Steitz, T. A. (1997)-Metals, motifs, and recognition in the crystal structure of a 5S rRNA domain, *Cell 91*, 705−712.
68. Kulinski, T., Bratek-Wiewiorowska, M. D., Zielenkiewicz, A., and Zielenkiewicz, W. (1997) Mg^{2+} dependence of the structure and thermodynamics of wheat germ and lupin seeds 5S rRNA, *J. Biomol. Struct. Dyn. 14*, 495−507.
69. Reblova, K., Spackova, N., Stefl, R., Csaszar, K., Koca, J., Leontis, N. B., and Sponer, J. (2003) Non-Watson−Crick basepairing and hydration in RNA motifs: molecular dynamics of 5S rRNA loop E, *Biophys. J. 84*, 3564−3582.
70. Auffinger, P., Bielecki, L., and Westhof, E. (2004) Symmetric K^+ and Mg^{2+} ion-binding sites in the 5S rRNA loop E inferred from molecular dynamics simulations, *J. Mol. Biol. 335*, 555−571.
71. VanLoock, M. S., Agrawal, R. K., Gabashvili, I. S., Qi, L., Frank, J., and Harvey, S. C. (2000) Movement of the decoding region of the 16S ribosomal RNA accompanies tRNA translocation, *J. Mol. Biol. 304*, 507−515.
72. Moazed, D., and Noller, H. F. (1987) Interaction of antibiotics with functional sites in 16S ribosomal RNA, *Nature 327*, 389−394.
73. Spahn, C. M., Blaha, G., Agrawal, R. K., Penczek, P., Grassucci, R. A., Trieber, C. A., Connell, S. R., Taylor, D. E., Nierhaus, K. H., and Frank, J. (2001) Localization of the ribosomal protection protein Tet(O) on the ribosome and the mechanism of tetracycline resistance, *Mol. Cell 7*, 1037−1045.
74. Oehler, R., Polacek, N., Steiner, G., and Barta, A. (1997) Interaction of tetracycline with RNA: photoincorporation into ribosomal RNA of *Escherichia coli*, *Nucleic Acids Res. 25*, 1219−1224.
75. Murray, J. B., and Arnold, J. R. (1996) Antibiotic interactions with the hammerhead ribozyme: tetracyclines as a new class of hammerhead inhibitor, *Biochem. J. 317*, 855−860.
76. Rogers, J., Chang, A. H., von Ahsen, U., Schroeder, R., and Davies, J. (1996) Inhibition of the self-cleavage reaction of the human hepatitis delta virus ribozyme by antibiotics, *J. Mol. Biol. 259*, 916−925.
77. Cannone, J. J., Subramanian, S., Schnare, M. N., Collett, J. R., D'Souza, L. M., Du, Y., Feng, B., Lin, N., Madabusi, L. V., Muller, K. M., Pande, N., Shang, Z., Yu, N., and Gutell, R. R. (2002) The comparative RNA web (CRW) site: an online database of comparative sequence and structure information for ribosomal, intron, and other RNAs, *BMC Bioinf. 3*, 2.

BI048533Y